Journal of
Applied Physics

Understanding modes of negative differential resistance in amorphous and polycrystalline vanadium oxides

Cite as: J. Appl. Phys. **128**, 244103 (2020); https://doi.org/10.1063/5.0027875
Submitted: 01 September 2020 . Accepted: 01 December 2020 . Published Online: 23 December 2020

Sanjoy Kumar Nandi, Sujan Kumar Das, Caleb Estherby, Angus Gentle, and Robert G. Elliman

COLLECTIONS

Paper published as part of the special topic on Phase-Change Materials: Syntheses, Fundamentals, and Applications

ARTICLES YOU MAY BE INTERESTED IN

Synthesis of vanadium dioxide thin films and nanostructures
Journal of Applied Physics **128**, 231101 (2020); https://doi.org/10.1063/5.0027690

Structural and electronic properties of monodomain ultrathin $PbTiO_3/SrTiO_3/PbTiO_3/SrRuO_3$ heterostructures: A first-principles approach
Journal of Applied Physics **128**, 244102 (2020); https://doi.org/10.1063/5.0031505

Threshold switching and electrical self-oscillation in niobium oxide films
Journal of Applied Physics **120**, 124102 (2016); https://doi.org/10.1063/1.4963288

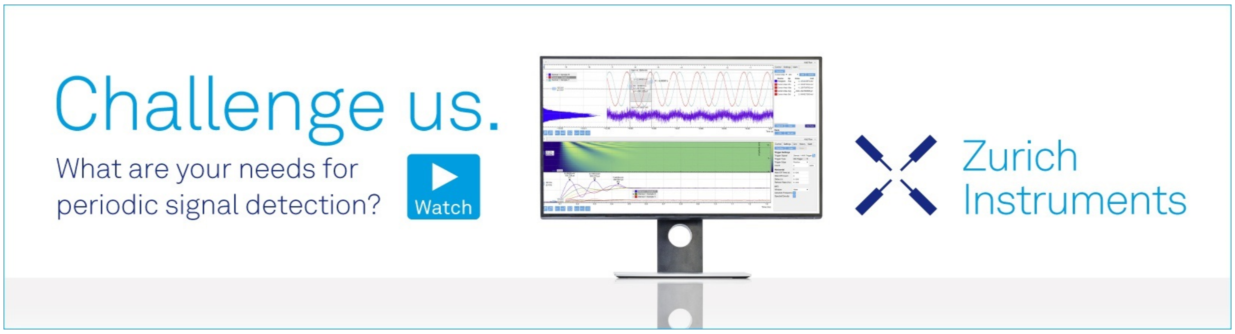

AIP Publishing

Journal of Applied Physics ARTICLE scitation.org/journal/jap

Understanding modes of negative differential resistance in amorphous and polycrystalline vanadium oxides

Cite as: J. Appl. Phys. **128**, 244103 (2020); doi: 10.1063/5.0027875
Submitted: 1 September 2020 · Accepted: 1 December 2020 ·
Published Online: 23 December 2020

View Online Export Citation CrossMark

Sanjoy Kumar Nandi,[1,a)] Sujan Kumar Das,[1,2] Caleb Estherby,[3] Angus Gentle,[3] and Robert G. Elliman[1]

AFFILIATIONS

[1] Department of Electronic Materials Engineering, Research School of Physics, The Australian National University, Canberra, ACT 2601, Australia
[2] Department of Physics, Jahangirnagar University, Dhaka, Bangladesh
[3] School of Mathematical and Physical Sciences, University of Technology Sydney, Sydney, NSW 2007, Australia

Note: This paper is part of the Special Topic on Phase-Change Materials: Syntheses, Fundamentals, and Applications.

[a)] **Author to whom correspondence should be addressed:** sanjoy.nandi@anu.edu.au

ABSTRACT

Metal–oxide–metal devices based on amorphous VO_x are shown to exhibit one of two distinct negative differential resistance (NDR) characteristics depending on the maximum current employed for electroforming. For low compliance currents they exhibit a smooth S-type characteristic and have a temperature-dependent device resistance characterized by an activation energy of 0.25 eV, consistent with conduction in polycrystalline VO_2, while for high compliance currents they exhibit an abrupt snap-back characteristic and a resistance characterized by an activation energy of 0.025 eV, consistent with conduction in oxygen deficient VO_x. In both cases, the temperature dependence of the switching voltage implies that the conductivity change is due to the insulator–metal transition in VO_2. From this analysis, it is concluded that electroforming at low currents creates a conductive filament comprised largely of polycrystalline VO_2, while electroforming at high currents creates a composite structure comprised of VO_2 and a conductive halo of oxygen deficient VO_x. The effect of electroforming on the NDR mode is then explained with reference to a lumped element model of filamentary conduction that includes the effect of a parallel resistance created by the halo. These results provide new insight into the NDR response of vanadium-oxide-based devices and a basis for designing devices with specific characteristics.

I. INTRODUCTION

Current-controlled negative differential resistance (NDR) in metal–oxide–metal (MOM) devices is of interest as the basis of nanoscale relaxation oscillators for use as solid-state neurons in neuromorphic computing arrays.[1–4] The as-fabricated devices are generally in a high resistance state and require a one-off electroforming step to initiate the NDR response.[5–7] This is typically achieved by subjecting the film to a voltage or current stress sufficient to form a filamentary conduction path through the film (i.e., soft dielectric breakdown), a process mediated by the generation, drift, and diffusion of atoms and ions in response to the applied electric field and local Joule heating.[8,9] The size, resistance, and stability of the resulting filaments depend critically on the forming conditions, and particularly on the maximum forming current and the associated temperature rise caused by Joule heating.[10,11] The high temperatures associated with electroforming can also cause crystallization of amorphous films and compositional or structural changes at the oxide/electrode interface that affect the final state of the electroformed device and its switching characteristics.[12–14] As a consequence, understanding the details of the electroforming process is an essential requirement for developing devices with specific characteristics.

In amorphous vanadium-oxide-based devices, the NDR response is generally attributed to the insulator–metal transition (IMT) in VO_2 on the assumption that this phase is crystallized within the filamentary conduction path during electroforming.[12]

Such devices generally exhibit smooth S-type NDR due to the heterogeneous nature of the IMT transition and the evolution of the temperature distribution during current-controlled testing.[15] However, they can also exhibit an abrupt snap-back characteristic under certain conditions, similar to that observed in NbO$_x$-based devices.[10,16] This novel NDR mode has the potential to offer new device functionality but its origin continues to be debated.[16,17]

In this study, we show that electroforming can be used to control the NDR characteristics of amorphous VO$_x$ films (a-VO$_x$) and that the snap-back response can result from changes in the filament microstructure and its impact on the effective circuit of the device. Significantly, this demonstrates that the observation of an abrupt conductivity change observed under current-controlled testing is insufficient to conclude the existence of an insulator–metal transition (IMT).

II. EXPERIMENTAL DETAILS

Two device structures were employed for these studies: metal–oxide–metal (MOM) capacitor structures fabricated with a common bottom electrode (BE) and a top electrode (TE) of 100 μm diameter circles defined by a shadow mask and cross-point devices ($2 \times 2\,\mu\text{m}^2$ - $20 \times 20\,\mu\text{m}^2$) fabricated using step-by-step photolithography, as shown in Fig. 1.[18] In both cases, the devices were fabricated on thermally oxidized (100 nm SiO_2) Si wafers by sequential layer deposition. The bottom electrodes consisted of a 10 nm-thick Ti adhesion layer and a 50 nm-thick Pt contact layer deposited by sequential e-beam evaporation. A 70 nm-thick functional oxide layer of either amorphous VO$_x$ or polycrystalline VO_2 was then deposited by reactive sputter deposition from a V target using an O_2/Ar ambient maintained at a pressure of 2.3 (or 1.5) mTorr using Ar/O_2 flow rates of 58/2 (or 58/10) sccm. Amorphous VO$_x$ films (a-VO$_x$) were achieved by maintaining the substrates at room temperature, and polycrystalline VO_2 films (pc-VO_2) were achieved by post-annealing the film at 450 °C in in a partial vacuum (1.5 Torr air). The devices were completed by adding top electrodes consisting of a 5 nm-thick Ti layer and a 25 nm Pt layer.

The as-deposited oxide films were characterized by grazing incident angle x-ray diffraction (GI-XRD), atomic force microscopy (AFM), Raman spectroscopy (RS), and electron Rutherford backscattering spectrometry (ERBS).[19] Electrical measurements were performed with an Agilent B1500A semiconductor parameter analyzer attached to a Signatone probe station (S-1160) and were undertaken in air by applying voltages to the top electrode while grounding the bottom electrode.

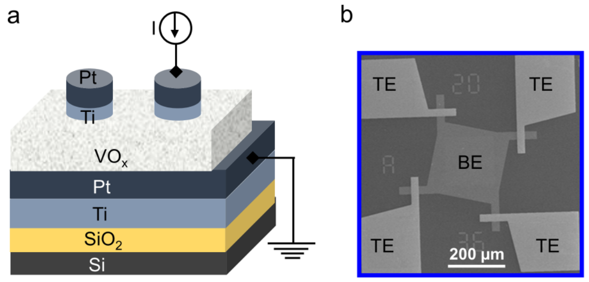

FIG. 1. (a) Schematic showing the test structure of Pt/Ti/a-VO$_x$/Pt devices and (b) scanning electron microscopy image of Pt/Ti/pc-VO_2/Pt cross-point device showing four $20 \times 20\,\mu\text{m}^2$ devices with a common bottom electrode.

III. EXPERIMENTAL RESULTS AND DISCUSSION

A. Composition and structure of films

Figure 2 shows GI-XRD spectra and AFM images of the as-deposited a-VO$_x$ and pc-VO_2 films, together with Raman spectra from the pc-VO_2 film as a function of temperature. The GI-XRD spectrum from the pc-VO_2 film has peaks corresponding

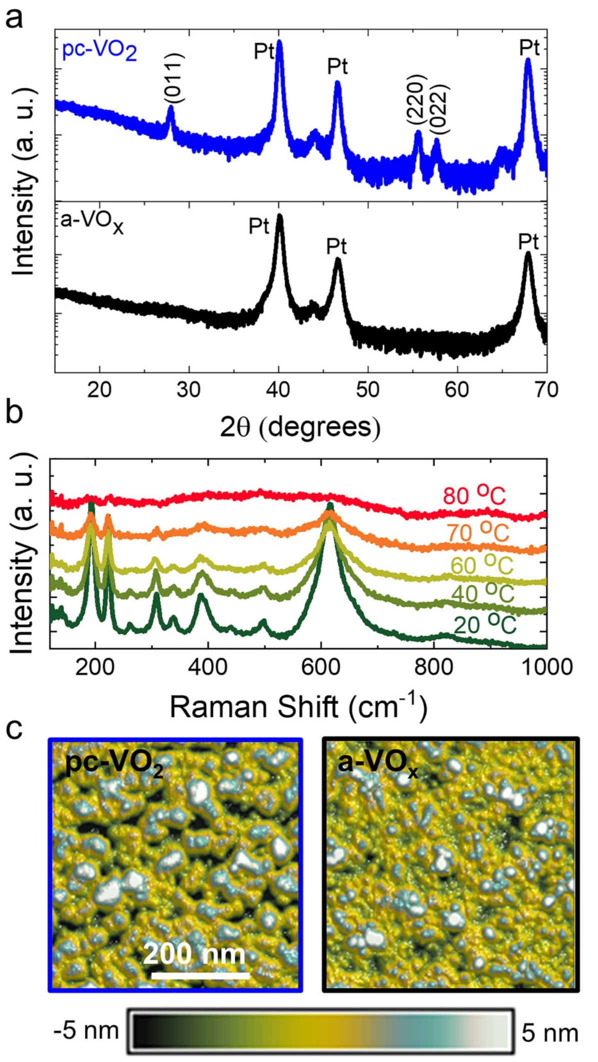

FIG. 2. (a) GI-XRD of pc-VO_2 and a-VO$_x$ films deposited on Pt, (b) Raman spectra from pc-VO_2 as a function of temperature, and (c) AFM images of the pc-VO_2 and a-VO$_x$ films.

to the (011), (220), and (022) planes of monoclinic VO_2, while that from an a-VO_x film is essentially featureless, consistent with the film being amorphous. (The only diffraction peaks observed in this case are from the underlying Pt substrate.) Temperature-dependent Raman analysis showed that the pc-VO_2 film underwent a thermally induced phase transition at temperatures between 40 °C and 80 °C, consistent with the well-known insulator–metal phase transition in VO_2. The surface morphology and roughness of the films was determined from AFM images and was similar for both films, with the RMS roughness measured to be 2.1 and 2.3 nm for the a-VO_x and pc-VO_2 films, respectively. These results combined with ERBS analysis show that the pc-VO_2 films are polycrystalline and composed of monoclinic VO_2, while the VO_x films are amorphous and have a composition close to V_2O_5 (i.e., $x \sim 2.5$).

B. Electrical characterization

As-fabricated devices were highly resistive, with resistances of order of several MΩ, and required a one-off electroforming step to initiate threshold switching, as shown in Fig. 3. This was achieved by scanning either the voltage or the current and detecting the abrupt conductivity change indicative of filament formation, and typically reduced the device resistance by around an order of magnitude, consistent with the creation of a filamentary conduction path in the oxide layer. For voltage-controlled electroforming, the maximum current (I_{CC}) was limited to avoid device damage. Immediately following electroforming, the devices exhibited symmetric threshold switching under voltage-controlled testing, with threshold voltages in the range from ±0.45 V to ±2.2 V. The switching times were measured to be ∼100 ns for the on-time (high-to-low resistance) and

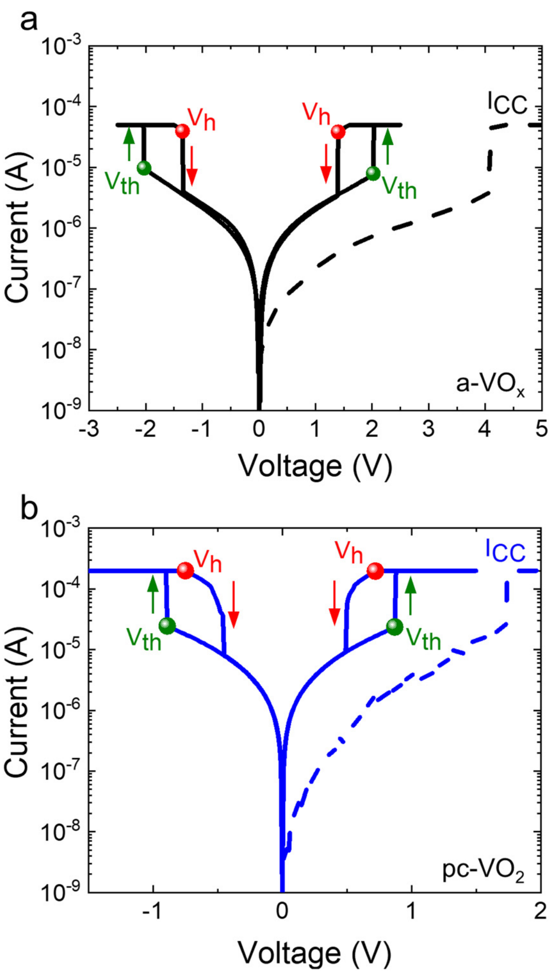

FIG. 3. Electroforming (dashed line) and subsequent threshold switching characteristics (solid line) for (a) an a-VO_x capacitor structure (100 μm diameter) and (b) a pc-VO_2 cross-point device (2 × 2 μm^2).

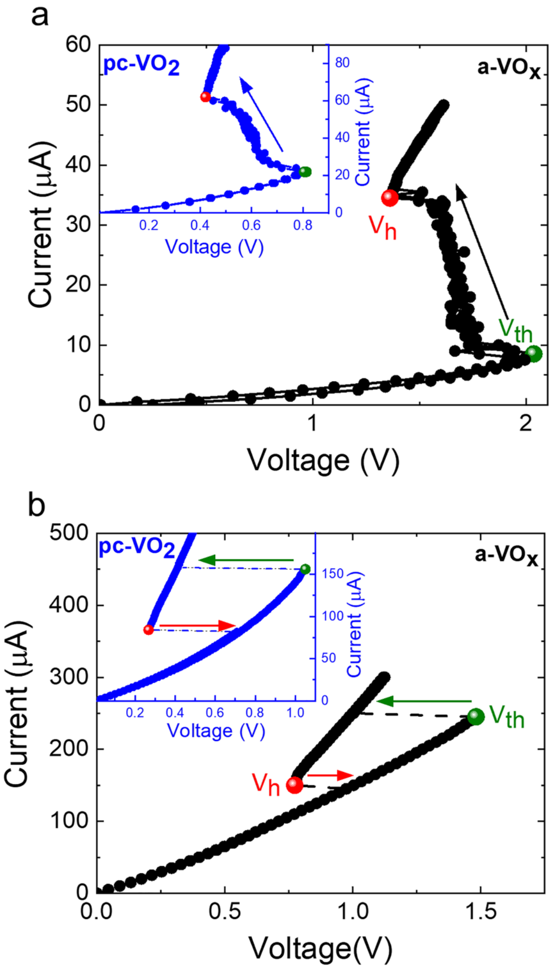

FIG. 4. (a) S-type NDR in an a-VO_x capacitor structure and inset showing similar behavior in a 2 × 2 μm^2 pc-VO_2 cross-point device. (b) Snap-back NDR characteristics an a-VO_x capacitor structure and inset showing similar behavior in a 5 × 5 μm^2 pc-VO_2 cross-point device.

~10 ns for the off-time (low to high resistance) for both device types. However, these measurements were limited by the RC time constant associated with the devices and the measurement system and do not reflect the intrinsic switching speed of the functional oxide. Similar behavior has previously been reported in both lateral and vertical device structures and is generally attributed to the thermally induced IMT in VO_2 and the associated positive feedback created by Joule heating.[20–22] In the case of a-VO_x devices, this is predicated on the assumption that the VO_2 phase is crystallized within the amorphous film during electroforming.[12]

Figure 4(a) shows corresponding current-controlled *I*–*V* characteristics for these devices. In this case, the current is constrained by the measurement system so that the increase in conductivity is self-limiting and the *I*–*V* characteristics vary continuously and the regions of NDR reflect the fact that the conductivity increases superlinearly with the current (temperature).[23] Given the significant difference in the initial film properties and device structures, the characteristics of the pc-VO_2 and a-VO_x devices are remarkably similar, reflecting the filamentary nature of the conduction process and the common origin of the conductivity change.

Of particular interest in this study is the fact that these devices can also exhibit a discontinuous "snap-back" characteristic, such as that shown in Fig. 4(b). This is an alternative switching mode characterized by an abrupt increase in conductivity as the current reaches a threshold value and an abrupt reduction in conductivity as it is reduced below a hold value. For the cases shown in Fig. 4(b), this hysteretic snap-back mode was effected by increasing the device area of the pc-VO_2 cross-point device from $4\,\mu m^2$ to $25\,\mu m^2$, and by increasing the electroforming compliance current for the a-VO_x capacitor structure. In both cases, the transition is associated with a reduction in the device resistance, but this alone does not explain the origin of the snap-back response.

C. Temperature dependence

To gain further insight into these switching modes, *I*–*V* characteristics were also investigated as a function of temperature, and Fig. 5 shows typical results. The sub-threshold *I*–*V* characteristics of both pc-VO_2 and a-VO_x devices are well modeled by a trap-limited conduction model (e.g., Poole–Frenkel conduction[24]), while voltage-controlled threshold switching and current-controlled snap-back characteristics of a-VO_x devices serve to illustrate the systematic reduction of the threshold voltages (V_{th}) and hold voltages (V_h) with increasing temperature. The inset in Fig. 5(b) also highlights the presence of discrete resistance changes during the metal to insulator transition, as previously reported for both thermal and voltage cycling of VO_2 devices where it was attributed to the heterogeneous nature of the transition.[15,25]

Results from such measurements are summarized in Fig. 6, which shows the temperature dependence of V_{th} and an Arrhenius plot of the sub-threshold device resistance for selected pc-VO_2 and a-VO_x devices. For switching based on a thermally induced metal–insulator transition, V_{th} is expected to decrease with increasing device temperature (T_0) due to the fact that the transition temperature (T_{IMT}) can be achieved at lower power.[26,27] In this case, the filament temperature (T) can be approximated by a lumped element model such that $T = T_0 + R_{therm}IV$, where R_{therm} is the thermal resistance of the filament, I is the device current, and V is the device voltage. Using Ohm's law and assuming a thermally activated device resistance of the form $R = R_0 e^{E_a/kT}$ then reveals that $V_{th}^2 = \frac{R_0}{R_{therm}}(T_{IMT} - T_0)e^{E_a/kT_{IMT}}$, i.e., V_{th}^2 scales linearly with the device temperature T_0 and goes to zero as T_0 approaches T_{IMT}. As shown in Fig. 6(a), the measured V_{th} for pc-VO_2 and a-VO_x devices satisfies this equation and has an intercept in the range of 340–350 K, consistent with the IMT in VO_2.[25,28] Significantly, this temperature is similar for pc-VO_2 and a-VO_x devices that exhibit continuous S-type NDR and for the a-VO_x device that exhibits abrupt snap-back characteristics. This confirms the role of VO_2 in the switching of a-VO_x devices and suggests that both the S-type and snap-back characteristics have a common origin.

The associated Arrhenius plot shows that the change in sub-threshold resistance of the devices that exhibit S-type NDR is well characterized by a single activation energy of ~0.25 eV, consistent with previously reported values for conduction in

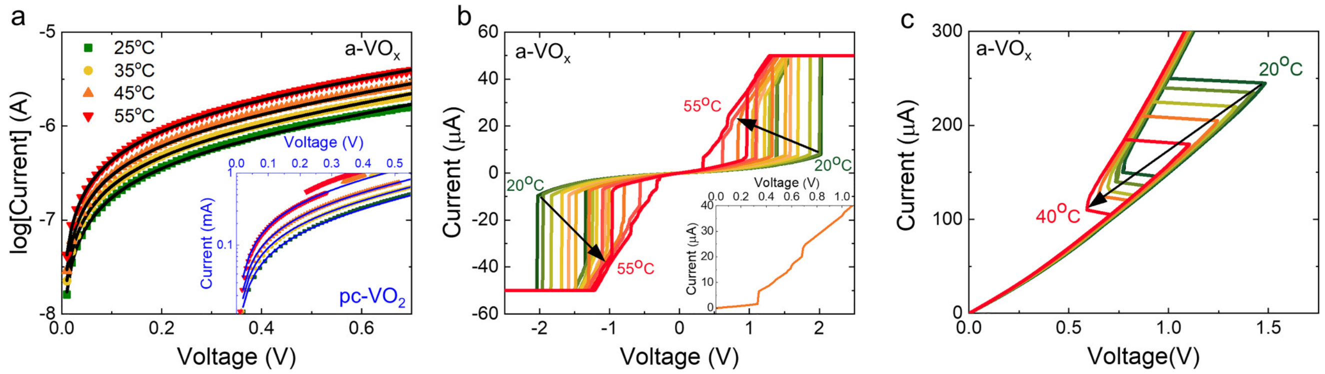

FIG. 5. (a) Sub-threshold *I*–*V* characteristics of a post-formed a-VO_x capacitor structure as a function of temperature, and inset showing similar behavior for a $5 \times 5\,\mu m^2$ pc-VO_2 cross-point device; (b) voltage-controlled threshold switching response of an a-VO_x device as a function of temperature; and (c) current-controlled NDR response of an a-VO_x device as a function of temperature.

polycrystalline VO_2.[29,30] This further reinforces the view that VO_2 is the dominant phase in both a-VO_x and pc-VO_2 devices. However, the sub-threshold resistance of the a-VO_x device that exhibits a snap-response is characterized by an activation energy of ∼0.025 eV, similar to that observed for the low resistance state of oxide-based resistive switching devices following an electroforming or a "set" operation.[31] The low activation energy in these cases reflects the high concentration of oxygen vacancies, and this is particularly revealing as it suggests that sub-threshold conduction is dominated by a high conductivity path through the oxide film even though the device exhibits a switching response characteristic of the IMT in VO_2.

D. Proposed model

Both pc-VO_2 and a-VO_x devices were shown to exhibit two distinct modes of CC-NDR, a smooth S-type mode or an abrupt snap-back mode, with the dominant switching mode dependence on the device area and the electroforming conditions. To understand this behavior, we draw on results from parallel studies of NbO_x-based devices where the NDR is attributed to the temperature dependence of trap-assisted conduction (e.g., Poole–Frenkel conduction[10,16,32]).

Using NbO_x devices as a prototypic example of filamentary threshold switching, we showed that the snap-back mode of CC-NDR can arise from a current redistribution process in which the current flowing in the region surrounding the conductive filament abruptly concentrates within the filament as it exhibits NDR in response to local Joule heating.[10] This can be understood by representing the device by a core–shell structure in which the core represents the high conductivity filament and the shell represents the parallel resistance due to conduction in the surrounding film. A simple circuit analysis then shows that current redistribution is controlled by the relative magnitudes of the NDR of the core, R_{NDR}, and the resistance of the shell, R_S, with continuous S-type characteristics observed for $R_s > R_{NDR}$ and abrupt snap-back characteristics observed for $R_s < R_{NDR}$.[16] This implies that the current in the surrounding area must be comparable to that in the filament in order to observe the snap-back response and highlights the fact that the dominant behavior will depend on the resistivity, thickness and area of the oxide film. Significantly, this analysis is independent of the process responsible for NDR.

In the present case, pc-VO_2 films were found to be much more conductive than a-VO_x films and, as a consequence, the device resistance of $2 \times 2\,\mu m^2$ pc-VO_2 cross-point devices was comparable to that of $100\,\mu m$ diameter a-VO_x capacitor structures. In both cases, these devices exhibited continuous S-type NDR when electroformed using low compliance currents. However, when the area of the pc-VO_2 cross-point devices was increased to $5 \times 5\,\mu m^2$ (a factor of 6.25), they exhibited a snap-back response, and when the $100\,\mu m$ diameter a-VO_x capacitor structures were electroformed using high compliance currents, they exhibited a similar response. Within the framework of the core–shell model, the behavior of the pc-VO_2 cross-point devices can be understood by accounting for the effect of the device area on the magnitude of the shell resistance, R_s, i.e., for the small area devices $R_s > R_{NDR}$ and the devices exhibit continuous S-type characteristics, while for the large area devices $R_s < R_{NDR}$ and they exhibit snap-back characteristics. Indeed, similar behavior has previously been reported for NbO_x devices.[8,10,16]

The effect of electroforming on a-VO_x devices requires further explanation. In this case, the device area was fixed and it is tempting to attribute the snap-back response to a change in R_{NDR}. However, we have found no clear correlation between R_{NDR} and the electroforming conditions. Instead, we refer to the temperature-dependent measurements in Fig. 6, which show that sub-threshold conduction in a-VO_x devices electroformed using high compliance currents is characterized by an activation energy of 0.025 eV, much lower than the 0.25 eV observed for devices formed at low compliance currents and for pc-VO_2 devices. Despite this, the NDR response of the devices remains consistent with the IMT in VO_2. This suggests that the filamentary conduction is no longer limited confined to a volume of pc-VO_2 but includes a parallel path of more conductive VO_x characterized by an activation energy of

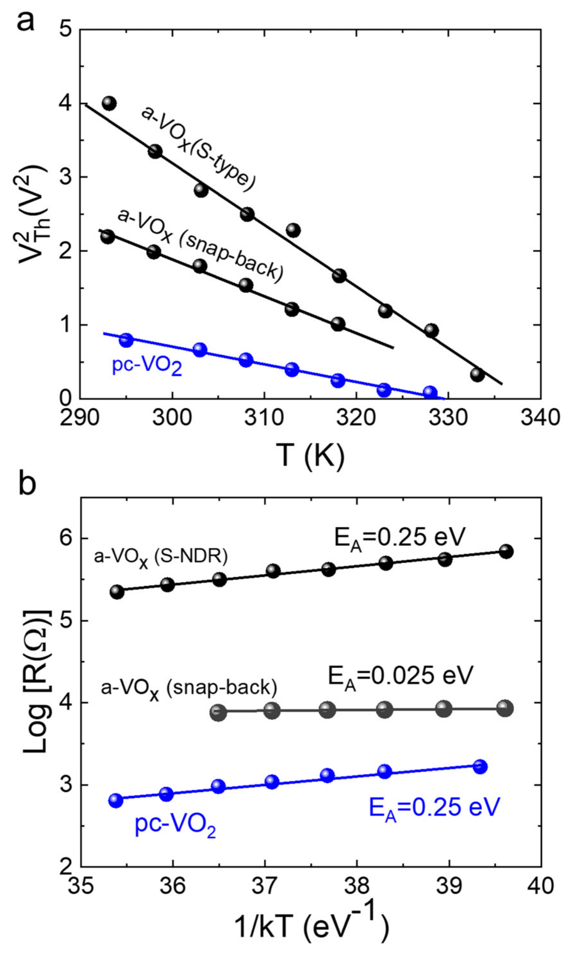

FIG. 6. (a) Temperature dependence of the threshold voltage and (b) an Arrhenius plot of the sub-threshold resistance for a-VO_x devices that exhibit S-type and snap-back NDR and for a $5 \times 5\,\mu m^2$ pc-VO_2 device that exhibits snap-back NDR.

0.025 eV. Such a structure can be understood by noting that the temperature distribution around the filament during electroforming has a strong radial dependence that will be reflected in the composition and structure of the oxide in this region. As crystallization occurs more rapidly at higher temperatures, the filament is expected to consist of a central VO_2-rich core and a halo of substoichiometric $VO_{x-\delta}$.[13,33] The effect of the electroforming can then be understood on the basis that the relative sizes of the VO_2 core and $VO_{x-\delta}$ halo depend on the compliance current, with low currents producing filaments that are dominated by pc-VO_2 and high compliance currents producing filaments with pc-VO_2 core and a significant $VO_{x-\delta}$ halo.

Figure 7 shows schematic representations of the proposed filament structures in a-VO_x devices electroformed with "low" and "high" compliance currents, together with an equivalent electrical circuit. The relative diameters of the core and halo regions are assumed to increase with increasing forming current, consistent with the observed reduction in filament resistance and its temperature dependence. From an electrical perspective, the device can then be considered as three parallel resistors: one associated with the core and having a temperature-dependent resistance governed by the heterogeneous IMT of VO_2 [represented in Fig. 7(c) by a "memristor" symbol]; the second with the halo region and having a resistance determined by the electroforming conditions; and the third with the surrounding film and having a resistance determined by the stoichiometry, thickness, and area of the oxide film. To a reasonable approximation, the resistance of the halo and the surrounding film can be treated as constants (i.e. fixed resistors) so that the model reduces to the core–shell model discussed earlier, with the core represented by a temperature-dependent resistor and the shell by a fixed parallel resistor of magnitude: $R_s = \frac{R_h R_f}{R_h + R_f}$, where R_h is the effective resistance of the filament halo and R_f is the effective resistance of the surrounding film. Based on this model, the observation that the a-VO_x devices exhibit S-type NDR at low compliance currents and snap-back NDR at high compliance currents can also be a attributed to a change in R_s, albeit from change in the halo resistance as a result of electroforming rather than a change in device area.

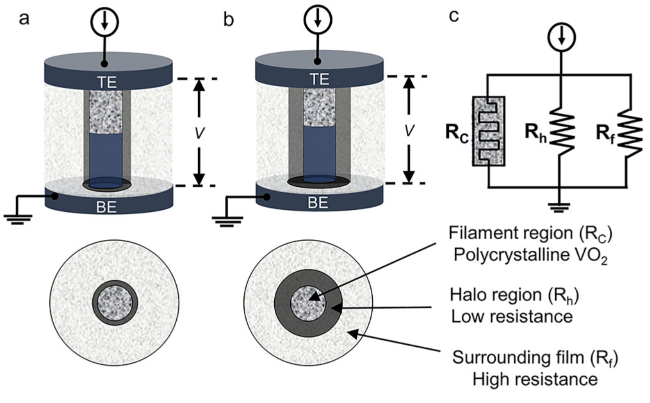

FIG. 7. Schematic of the proposed filamentary core–shell structure produced by electroforming at (a) low and (b) high compliance currents and (c) the equivalent circuit model.

IV. SUMMARY AND CONCLUSIONS

The voltage-controlled threshold switching and current-controlled NDR behavior of electroformed a-VO_x and pc-VO_2 devices were investigated. Temperature-dependent electrical measurements were consistent with the IMT in VO_2 and with the crystallization of this phase within the a-VO_x films during electroforming. Following electroforming, each device type exhibited two distinct modes of NDR, a continuous S-type response and an abrupt snap-back response, depending on the device area and electroforming conditions. This behavior was interpreted with reference to a simple core–shell model of filamentary conduction in which the core represented the high conductivity filament and the shell represented a parallel resistance due to the surrounding film. This predicted a transition between the S-type and snap-back behavior based on the relative magnitudes of the negative differential resistance and the shell resistance. For pc-VO_2 devices, the transition was demonstrated by using the device area to vary the shell resistance, as previously reported for a-NbO_x devices. However, in the case of a-VO_x devices, it was controlled by the electroforming conditions. In that case, electroforming with high compliance currents was shown to produce composite filaments that were characterized by a high conductivity and weak temperature dependence at sub-threshold current but by the IMT of VO_2 at high currents. This was represented by a pc-VO_2 core and a surrounding substoichiometric halo, with the high conductivity halo acting to reduce the overall shell resistance and thereby control the transition between S-type and snap-back modes. Significantly, these results show that the snap-back characteristic is a generic response of systems that exhibit NDR. The advantages of crystalline or amorphous vanadium oxides for threshold switching applications is inconclusive as both a-VO_x and pc-VO_2 have limitations. For example, electroforming-free, reliable threshold switching in p-VO_2 can be achieved by engineering the device geometry (device area, thickness of the oxide films, etc.) with an important drawback of lower transition temperature (340 K).[34] Conversely, electroformed a-VO_x devices show low yield and high device-to-device variability, as the size, resistance, and stability of the resulting filaments depend critically on the forming conditions, and particularly on the maximum forming current and associated temperature rise caused by Joule heating.[35–37] In a recent study, Rupp *et al.*[38] showed that doping (e.g., Cr) in a-VO_x can induce athermal switching with higher thermal stability (~365 K). This suggests that further work is required to improve the reliability and endurance of a-VO_x-based devices.

ACKNOWLEDGMENTS

This work was partly funded by the Australian Research Council (ARC) and Varian Semiconductor Equipment/Applied Materials through an ARC Linkage Project Grant (No. LP150100693). We would like to acknowledge access to NCRIS facilities at the ACT node of the Australian National Fabrication Facility (ANFF) and the Australian Facility for Advanced ion-implantation Research (AFAiiR) and thank Dr. Tom Ratcliff for comments and feedback on the manuscript. We would also like to thank James Murray for Raman analysis and Shimul Kanti Nath for the assistance during device processing and discussion on switching behavior. Caleb Estherby would like to acknowledge the Australian Government Research Training Program Scholarship.

DATA AVAILABILITY

The data that support the findings of this study are available from the corresponding author upon reasonable request.

REFERENCES

[1] M. D. Pickett, G. Medeiros-Ribeiro, and R. S. Williams, Nat. Mater. **12**(2), 114 (2013).

[2] R. Tobe, M. S. Mian, and K. Okimura, J. Appl. Phys. **127**(19), 195103 (2020).

[3] A. Velichko, M. Belyaev, V. Putrolaynen, A. Pergament, and V. Perminov, Int. J. Mod. Phys. B **31**(2), 1650261 (2017).

[4] N. Shukla, W.-Y. Tsai, M. Jerry, M. Barth, V. Narayanan, and S. Datta, in *2016 IEEE Symposium on VLSI Technology* (IEEE, 2016).

[5] C. Nauenheim, C. Kuegeler, A. Ruediger, and R. Waser, Appl. Phys. Lett. **96**(12), 122902 (2010).

[6] D. V. Morgan, M. J. Howes, R. D. Pollard, and D. G. P. Waters, Thin Solid Films **15**(1), 123–131 (1973).

[7] M. Son, X. Liu, S. M. Sadaf, D. Lee, S. Park, W. Lee, S. Kim, J. Park, J. Shin, S. Jung, M. Ham, and H. Hwang, IEEE Electron Device Lett. **33**(5), 718–720 (2012).

[8] S. K. Nandi, S. K. Nath, A. E. El-Helou, S. Li, T. Ratcliff, M. Uenuma, P. E. Raad, and R. G. Elliman, ACS Appl. Mater. Interfaces **12**, 8422 (2020).

[9] C. N. Berglund, IEEE Trans. Electron Devices **16**(5), 432–437 (1969).

[10] S. K. Nandi, S. K. Nath, A. E. El-Helou, S. Li, X. Liu, P. E. Raad, and R. G. Elliman, Adv. Funct. Mater. **29**(50), 1906731 (2019).

[11] J. M. Goodwill and M. Skowronski, J. Appl. Phys. **126**(3), 035108 (2019).

[12] X. Zhou, D. Gu, Y. Li, H. Qin, Y. Jiang, and J. Xu, Nanoscale **11**(45), 22070–22078 (2019).

[13] L. Shuai, L. Xinjun, N. Sanjoy Kumar, and E. Robert Glen, Nanotechnology **29**(37), 375705 (2018).

[14] S. K. Nandi, X. Liu, D. K. Venkatachalam, and R. G. Elliman, Appl. Phys. Lett. **107**(13), 132901 (2015).

[15] Y. Sharma, J. Balachandran, C. Sohn, J. T. Krogel, P. Ganesh, L. Collins, A. V. Ievlev, Q. Li, X. Gao, and N. Balke, ACS Nano **12**(7), 7159–7166 (2018).

[16] S. Li, X. Liu, S. K. Nandi, S. K. Nath, and R. G. Elliman, Adv. Funct. Mater. **29**, 1905060 (2019).

[17] S. Kumar, J. P. Strachan, and R. S. Williams, Nature **548**(7667), 318 (2017).

[18] S. K. Nath, S. K. Nandi, S. Li, and R. G. Elliman, Appl. Phys. Lett. **114**(6), 062901 (2019).

[19] M. Vos, X. Liu, P. L. Grande, S. K. Nandi, D. K. Venkatachalam, and R. G. Elliman, Nucl. Instrum. Methods Phys. Res. Sect. B **340**, 58–62 (2014).

[20] M. S. Mian, K. Okimura, and J. Sakai, J. Appl. Phys. **117**(21), 215305 (2015).

[21] G. Seo, B.-J. Kim, H.-T. Kim, and Y. W. Lee, Curr. Appl. Phys. **14**(9), 1251–1256 (2014).

[22] D. Li, A. A. Sharma, N. Shukla, H. Paik, J. M. Goodwill, S. Datta, D. G. Schlom, J. A. Bain, and M. Skowronski, Nanotechnology **28**(40), 405201 (2017).

[23] G. A. Gibson, Adv. Funct. Mater. **28**(22), 1704175 (2018).

[24] D. Ielmini and Y. Zhang, J. Appl. Phys. **102**(5), 054517 (2007).

[25] J. A. J. Rupp, M. Querré, A. Kindsmüller, M.-P. Besland, E. Janod, R. Dittmann, R. Waser, and D. J. Wouters, J. Appl. Phys. **123**(4), 044502 (2018).

[26] F. Chudnovskii, Zh. Tekh. Fiz. **45**, 1561–1583 (1975).

[27] A. Bugaev, B. Zakharchenia, and F. Chudnovskii, The metal-semiconductor phase transition and its application (Leningrad Izdatel Nauka, 1979).

[28] K. Okimura, N. Hanis Azhan, T. Hajiri, S.-i. Kimura, M. Zaghrioui, and J. Sakai, J. Appl. Phys. **115**(15), 153501 (2014).

[29] V. A. Blagojević, N. Obradović, N. Cvjetićanin, and D. M. Minić, Sci. Sintering **45**(3), 305–311 (2013).

[30] M. J. Tadjer, V. D. Wheeler, B. P. Downey, Z. R. Robinson, D. J. Meyer, C. R. Eddy, Jr., and F. J. Kub, Solid State Electron. **136**, 30–35 (2017).

[31] X. Liu, S. K. Nandi, D. K. Venkatachalam, S. Li, K. Belay, and R. G. Elliman, in 2014 Conference on Optoelectronic and Microelectronic Materials and Devices, Perth, Australia, 14–17 December 2014.

[32] S. Slesazeck, H. Mähne, H. Wylezich, A. Wachowiak, J. Radhakrishnan, A. Ascoli, R. Tetzlaff, and T. Mikolajick, RSC Adv. **5**(124), 102318–102322 (2015).

[33] Y. Ma, J. M. Goodwill, D. Li, D. A. Cullen, J. D. Poplawsky, K. L. More, J. A. Bain, and M. Skowronski, Adv. Electron. Mater. **5**(7), 1800954 (2019).

[34] W. Yi, K. K. Tsang, S. K. Lam, X. Bai, J. A. Crowell, and E. A. Flores, Nat. Commun. **9**(1), 1–10 (2018).

[35] D. Kalaev, E. Yalon, and I. Riess, Solid State Ionics **276**, 9–17 (2015).

[36] J. J. Yang, F. Miao, M. D. Pickett, D. A. A. Ohlberg, D. R. Stewart, C. N. Lau, and R. S. Williams, Nanotechnology **20**(21), 215201 (2009).

[37] S. K. Nandi, X. Liu, D. K. Venkatachalam, and R. G. Elliman, Phys. Rev. Appl. **4**(6), 064010 (2015).

[38] J. Rupp, R. Waser, and D. Wouters, in *2016 IEEE 8th International Memory Workshop (IMW)* (IEEE, 2016).